Check for updates

Enhanced hydrogen evolution reaction performance of anatase–rutile TiO$_2$ heterojunction *via* charge transfer from rutile to anatase†

Nurul Affiqah Arzaee, [ab] Nuttapon Yodsin,[c] Habib Ullah, *[d] Sabiha Sultana,[de] Mohamad Firdaus Mohamad Noh,[ab] Ahmad Wafi Mahmood Zuhdi, [b] Abd Rashid Bin Mohd Yusoff,*[f] Siriporn Jungsuttiwong*[c] and Mohd Asri Mat Teridi *[a]

In light of recent doubts surrounding the industrial viability of photo(electro)catalysis technology for sustainable hydrogen production, it becomes imperative to align materials development with rationalized synthesis protocols. In this study, we present an innovative technique utilizing atmospheric-pressure chemical vapor deposition (APCVD) to rapidly produce TiO$_2$ in just 5 minutes using pure TiCl$_4$ as the sole reagent. The resulting photoanode exhibits exceptional photoelectrochemical (PEC) water-splitting performance, achieving a photocurrent density of 2.06 mA cm^{-2} at 1.23 V RHE. Moreover, the photoanode demonstrates sustained operation for 16 hours, leading to the successful collection of 138 μmol of H$_2$ and 62 μmol of O$_2$. These remarkable results are attributed to the controlled formation of an anatase–rutile phase-junction, the presence of well-balanced oxygen vacancies, and the bifrustum nanoparticle–nanoflake structure with a unique light trapping effect and large surface area. Density functional theory calculations confirm that the water-splitting reaction primarily occurs at undercoordinated Ti and O atoms in both anatase and rutile TiO$_2$. Notably, the calculated Gibbs free energy values for the hydrogen evolution reaction (HER) differ significantly between rutile (−0.86 eV) and anatase TiO$_2$ (0.22 eV). In the heterojunction, charge transfer enhances the HER performance through shared electronic density, resulting in a synergistic effect that surpasses the capabilities of individual surfaces and underscores the importance of electronic interactions within the junction.

Introduction

Photoelectrochemical (PEC) water splitting using semiconductors as photoelectrodes has been considered a

[a] *Solar Energy Research Institute, Universiti Kebangsaan Malaysia, 43600 Bangi, Selangor, Malaysia. E-mail: asri@ukm.edu.my; Tel: +603 8911 8580*

[b] *Institute of Sustainable Energy (ISE), Universiti Tenaga Nasional (UNITEN), Jalan IKRAM-UNITEN, 43000 Kajang, Selangor, Malaysia*

[c] *Center for Organic Electronics and Alternative Energy, Department of Chemistry and Center for Innovation in Chemistry, Faculty of Science, Ubon Ratchathani University, Ubon Ratchathani 34190, Thailand. E-mail: siriporn.j@ubu.ac.th; Tel: +66 8 1692 4610*

[d] *Department of Engineering, Faculty of Environment, Science and Economy, University of Exeter, Penryn Campus, Cornwall TR10 9FE, UK. E-mail: hu203@exeter.ac.uk*

[e] *Physics Department, Faculty of Science, Universiti Teknologi Malaysia, 81310, Johor Bahru, Johor, Malaysia*

[f] *Department of Chemical Engineering, Pohang University of Science and Technology (POSTECH), 77 Cheongam-Ro, Nam-Gu, Pohang 37673, Republic of Korea. E-mail: abdr@khu.ac.kr*

† Electronic supplementary information (ESI) available. See DOI: https://doi.org/10.1039/d3cy00918a

promising route to generate renewable hydrogen fuel.[1,2] To achieve sustainable production of hydrogen, it is critical to develop an energy-efficient fabrication process for the photoelectrode material. Specifically, the process must be designed in a way that production time and chemical use are minimized. TiO$_2$ is chosen as a representative photoelectrode in this study due to the suitable band edge position, good stability and nontoxicity.[3,4] Nonetheless, TiO$_2$ still suffers from poor light absorption and high electron–hole recombination rate, which are responsible for the performance loss.[5,6] It is well documented that these limitations can be alleviated using various strategies such as by introducing an anatase–rutile junction[7–9] and oxygen vacancies in TiO$_2$.[7,10] The junction between the anatase and rutile phases is of particular interest in photocatalysis because it can facilitate the separation of photo-generated electron–hole pairs, leading to higher photocatalytic activity.[11]

Nevertheless, the fabrication of the anatase–rutile junction is rather complex and time-consuming. For instance, Yang and Wu developed anatase–rutile nanostructures using several synthesis techniques including hydrothermal and

This journal is © The Royal Society of Chemistry 2023

Catal. Sci. Technol., 2023, **13**, 6937–6950 | **6937**

solvothermal methods.[12] TiO_2 generated a photocurrent of 1.73 mA cm^{-2} at 1.23 V_{RHE}, but more than 40 hours was required to prepare the photoanode. Sutiono *et al.* fabricated the anatase–rutile TiO_2 *via* a hydrothermal method by placing the FTO substrate at the bottom of a Teflon-liner instead of leaning the FTO against the liner's wall.[13] Although a high photocurrent of 2.32 mA cm^{-2} at 1.23 V_{RHE} was recorded, at least 18.5 hours were needed to complete the fabrication process. A more complicated preparation process of anatase–rutile was reported by Wei *et al.* through the combination of hydrothermal method and atomic layer deposition, which produced photocurrent of only 2.08 mA cm^{-2} at 1.23 V_{RHE}.[14]

Meanwhile, introduction of oxygen vacancies in the TiO_2 photoanode is favorable for PEC activity as the defect increases the concentration of free carrier density[7] and provides high water adsorption sites.[10] However, the formation and tuning of oxygen vacancies usually involve post-treatments on pre-deposited TiO_2 films such as dipping in $NaBH_4$ (ref. 15) and annealing in N_2 or H_2 atmosphere.[14,16] The post-treatments have further extended the synthesis duration of pristine TiO_2. This means that the development of high-performance TiO_2 by combining the anatase–rutile and oxygen vacancy approaches is inefficient. Hence, a more realistic synthesis route is highly sought after to achieve a sustainable hydrogen generation *via* the TiO_2 photoanode.

In response to this, atmospheric pressure chemical vapor deposition (APCVD) has been demonstrated as an efficient and rapid synthesis approach for photoelectrodes, which is also convenient for large-scale processes.[17,18] Previous studies have successfully developed TiO_2 films with various dopants like boron, nitrogen, and fluorine using the APCVD method and the time taken for depositing the films was not more than 210 s.[18–20] However, the synthesized film consisted of only a single phase (either anatase or rutile) most likely due to the use of ethyl acetate as oxygen source and insufficient transformation temperature. The single phase is ineffective for charge separation in the photoelectrode. To partially convert the anatase phase to rutile phase, Kafizas *et al.* have applied an additional annealing process with a temperature of over 600 °C after preparing the TiO_2 by APCVD,[21] but this strategy defeats the purpose of developing a rapid fabrication method.

Here, we present for the first time the successful fabrication of a high-performance mixed-phase TiO_2 photoanode *via* APCVD in a very short timescale (5 minutes) using pure $TiCl_4$ as a sole reagent. A systematic parameter study for optimizing APCVD was performed to determine the optimum conditions to deposit TiO_2 with exceptional properties. Along with the appropriate concentration of oxygen vacancies and well-tuned film morphology, it is found that the coexistence of anatase and rutile phases naturally forms a staggered junction in the photoanode, which effectively suppresses the recombination of charge carriers. As a result, an impressive photocurrent density of 2.06 mA cm^{-2} at 1.23 V_{RHE} is obtained. Besides, the photoanode is highly reproducible with a small performance deviation and

exhibits a stable photocurrent over at least 16 h of operation time. The experimental data are validated with first principle density functional theory (DFT) simulations and the results proved that the water splitting reaction mechanism occurs at the undercoordinated Ti and O atoms in both anatase and rutile TiO_2. Overall, our findings provide one of the best solutions for the sustainable development of outstanding TiO_2 photoanodes.

Experimental section

Preparation of TiO_2 thin films

TiO_2 films were grown on FTO (TEC 8, Pilkington) using a custom-built APCVD system (Fig. S1†). Briefly, 1 ml $TiCl_4$ (99%, Merck) was inserted into the trap body of a two-piece glass cold trap and the trap body was capped with a trap finger. Two separate tubes were then connected to the joints of the trap finger, where the inner joint-sidearm was connected to an argon gas supply while the outer joint to a three-neck round-bottom flask (mixing chamber). The mixing chamber was also connected to a purified air supply and a glass tube connected to a covered hot plate (reaction chamber). Prior to the deposition process, FTO substrates were cleaned using an ultrasonic bath in acetone, methanol and 2-propanol (each for 10 min). The substrates were then rinsed under DI water and dried with a nitrogen stream. A substrate was placed on the preheated hot plate and the nozzle of the glass tube was positioned directly on top of the substrate. The deposition began by flowing argon and purified air at 90 and 1560 cm^3 min^{-1}, respectively. The process was carried out at 400, 500 and 600 °C for 5 min to investigate the phase changes. Correspondingly, the samples are denoted by TiO_2-400, TiO_2-500 and TiO_2-600. The morphology of the samples was studied by varying the distance between the nozzle and the FTO surface (2, 8 and 15 mm) as well as by controlling the deposition time (3, 5 and 7 min).

Characterization

The crystalline behavior of the films was explored using an X-ray diffractometer (XRD) (Bruker, D8 Advance). The mass fraction of anatase (W_a) and rutile (W_r) phases in each sample can be estimated from the XRD spectra using the following equations:

$$W_a = \frac{K_a A_a}{K_a A_a + A_r} \tag{1}$$

$$W_r = \frac{A_r}{K_a A_a + A_r} \tag{2}$$

where A_a and A_r represent the integrated intensities of anatase (101) and rutile (110) peaks, respectively. K_a is a correction coefficient, which is equal to 0.886.[22] X-ray photoelectron spectroscopy (XPS) was conducted using an Al Kα X-ray gun (Axis Ultra Kratos/Shimadzu) to determine the chemical bonding and elemental composition. The film

6938 | *Catal. Sci. Technol.*, 2023, **13**, 6937–6950

This journal is © The Royal Society of Chemistry 2023

phase was studied using a Raman spectrometer (Thermo Scientific, DXR2xi) equipped with a 532 nm wavelength laser. UV-vis light absorption spectra were obtained from a UV-visible spectrometer (Perkin Elmer Lambda 950). Field emission scanning electron microscopy (FESEM) (ZEISS Merlin) was employed to observe the morphology. The thickness and roughness of films were recorded from the respective profilometer (Bruker, D8 Advance) and atomic force microscopy (AFM) (Nanosurf Easyscan2). Hall measurement (Ecopia HMS5000) was used to analyze the electrical properties of FTO. Photoelectrochemical measurements were performed on an Autolab potentiostat/galvanostat (Metrohm, PGSTAT 204) in 0.5 M Na_2SO_4 electrolyte with a standard three-electrode electrochemical system composed of the prepared samples, platinum and Ag/AgCl as the working, counter and reference electrode, respectively. The samples were illuminated by a xenon lamp without any filter and adjusted to 100 mW cm^{-2} by a standard silicon reference cell from Daystar Meter. The potentials were converted to the reversible hydrogen electrode (E_{RHE}) scale according to the Nernst equation:[23–26]

$$E_{RHE} = E_{Ag/AgCl} + 0.059pH + E^0_{Ag/AgCl} \qquad (3)$$

where $E_{Ag/AgCl}$ is the experimentally measured potential *versus* Ag/AgCl, $E^0_{Ag/AgCl}$ is 0.209 V at 25 °C for an Ag/AgCl electrode in 3 M NaCl and electrolyte with pH of 7.0. The applied bias photon-to-current efficiency (ABPE) is calculated from LSV curves as follows:

$$ABPE = J \times \frac{1.23 - V_{RHE}}{P_{light}} \times 100\% \qquad (4)$$

where J, V_{RHE} and P_{light} represent the generated photocurrent density (mA cm^{-2}), applied potential *vs.* RHE (V) and incident light intensity (mW cm^{-2}), respectively. The H_2 and O_2 gases evolved during the test were collected and measured using water displacement technique. The volume of produced gas was determined every 4 h for a total duration of 16 h.

Density functional theory computations

The reaction mechanism of water splitting on the anatase TiO_2 (101) and rutile TiO_2 (110) was investigated using plane-wave based DFT calculations performed using the Vienna *Ab initio* Simulation Package (VASP). The projector-augmented wave (PAW)[27] with a generalized gradient approximation (GGA) refined by Perdew, Burke and Ernzerhof (PBE)[28] was used in the calculations. An energy convergence of 1×10^{-6} eV per cell, a force convergence of 1×10^{-2} eV Å^{-1} and an energy cut-off of 450 eV were employed in the calculations. A spin-unrestricted calculation was applied in all cases. An isolated gas molecule was calculated in a 15 Å × 15 Å × 15 Å box. A (2 × 2) slab of the anatase TiO_2 (101) and rutile TiO_2 (110) surfaces was separated from its replicas by 12 Å of vacuum. The anatase TiO_2 (101) and rutile TiO_2 (110) surfaces consist of 72 and 68 atoms with three Ti-layers, respectively.

Monkhorst–Pack grids of 5 × 5 × 1 were used for all TiO_2 systems. The electronic properties, *i.e.*, the density of states (DOS), was analyzed to understand the changes in the electronic properties of anatase TiO_2 (101) and rutile TiO_2 (110) surfaces. The adsorption energy (E_{ads}) was calculated from the following equation:

$$E_{ads} = E_{system} - E_{surface} - E_{isolated\ water} \qquad (5)$$

where E_{system} is the total energy of an adsorbate–TiO_2 complex. E_{suface} and $E_{isolated\ water}$ are the total energy of the bare TiO_2 surface and the total energy of an isolated water molecule, respectively. A negative E_{ads} value refers to the attractive interactions between the surface and water; alternatively, a more negative value relates to stronger adsorption interactions.

Results and discussion

Phase and defect modulation

The crystal phase and crystallographic defect concentration of TiO_2 films were tuned by annealing the films at 400, 500 and 600 °C. As shown by XRD analysis in Fig. 1a, TiO_2-400 exhibits characteristic peaks corresponding to pure anatase phase (JCPDS No. 21-1272).[29] Peaks belonging to FTO substrate are also identified in this sample, which might be due to the low film thickness. This could be correlated with the slow decomposition rate of $TiCl_4$ at low temperature. As the deposition temperature increases to 500 and 600 °C, the FTO diffraction peaks disappear, indicating that the TiO_2 film completely covers the underlying substrate.[30] Meanwhile, similar anatase peaks are observed in the TiO_2 deposited at higher temperatures. The intensity of XRD peaks also becomes stronger with the increase of temperature, suggesting that TiO_2 films with higher crystallinity are formed. On a closer view, the peak intensity of the (105) crystal plane reduces, while that of the (211) plane enhances as the films were subjected to higher temperature, reflecting the switch of the growth orientation.

Samples grown at 500 and 600 °C also exhibit new peaks, which are unambiguously assigned to the rutile phase (JCPDS No. 21-1276).[31] Furthermore, the increasing trend in the peak intensity of rutile with respect to deposition temperature is identical to that of anatase. Table S1† clearly shows that the mass fraction of rutile increases with increasing deposition temperature (0, 24 and 28 wt% for TiO_2 deposited at 400, 500 and 600 °C, respectively). In typical cases, the anatase phase starts to transform irreversibly to rutile phase in air at a temperature between 600 and 700 °C.[32,33] However, the transition temperature could become lower depending on the raw materials and processing methods used for the fabrication of TiO_2.[34] Besides, the phase transformation process is not instantaneous but rather time-dependent.[35] For these reasons, the TiO_2 prepared by APCVD shows mixed-phase at lower temperature of 500 °C.

This journal is © The Royal Society of Chemistry 2023

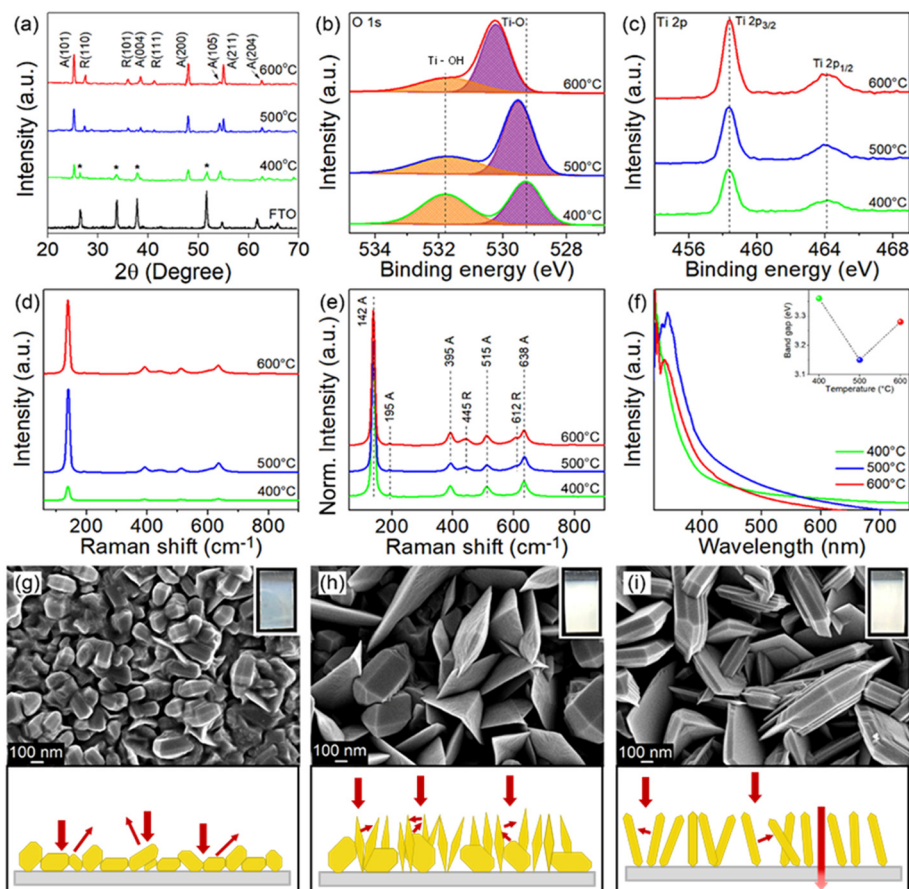*Catal. Sci. Technol.*, 2023, **13**, 6937–6950 | **6939**

Fig. 1 (a) XRD patterns (asterisk represents FTO), XPS spectra of (b) O 1s and (c) Ti 2p, (d) Raman spectra, (e) normalized Raman spectra and (f) UV-vis absorption spectra of TiO_2 prepared at different temperatures. Inset of (f) is the corresponding band gap. Top: FESEM and photographic images (inset) of TiO_2 deposited at (g) 400 °C, (h) 500 °C and (i) 600 °C. Bottom: Respective schematic illustrations of light–matter interaction in the films.

Considering the detection limitations of XRD, the concentration of crystallographic defects in the films was determined with XPS. The O 1s spectra in Fig. 1b show two peaks centered at 529.3 and 531.8 eV which are associated with the lattice oxygen bonded to Ti metal (Ti–O) and hydroxyl groups chemisorbed on Ti ions (Ti–OH) to reimburse the charge site of oxygen vacancies (V_O), respectively.[36] The peak intensity of Ti–OH obviously decreases when the deposition temperature increases from 400 to 600 °C, which indirectly indicates the suppressed V_O formation at high temperature. This is verified by estimating the ratio of V_O to lattice oxygen using Gaussian fitting on the Ti–OH and Ti–O peaks,[37,38] where the ratios of 1.03, 0.53 and 0.43 have been acquired for samples prepared at 400, 500 and 600 °C, respectively. Meanwhile, the Ti $2p_{3/2}$ and Ti $2p_{1/2}$ peaks detected at 458.3 and 464.1 eV signify the existence of Ti^{4+} (Fig. 1c).[7,39] Note that the electronic structure of Ti 2p does not change upon increasing the annealing temperature, despite the significant change of Ti–OH peaks (*i.e.*, change of oxygen vacancies in the samples).[39] Additionally, the broadening of the Raman peak in Fig. 1d particularly for TiO_2-400 is ascribed to the non-stoichiometric behavior of TiO_2. This result could confirm the presence of a high

density of oxygen vacancies in the film.[7,40] The intensity of the Raman peak was then normalized to investigate the phase transformation (Fig. 1e). The vibrational modes of the anatase phase of TiO_2 peaked at 142, 395, 515 and 638 cm^{-1}, which agree with the respective Raman active modes of E_{1g}, B_{1g}, A_{1g} and E_g and can be clearly observed in all films.[9,22,41] The Raman peak at 142 cm^{-1} is associated with the symmetric stretching vibration of the Ti–O–Ti bond, while peaks at 395 and 515 cm^{-1} are formed by the symmetric and anti-symmetric bending vibration of O–Ti–O in TiO_2, respectively.[22,42] In line with XRD, peaks attributed to rutile TiO_2 located at 445 (E_g) and 612 cm^{-1} (A_{1g}) appear only in TiO_2-500 and TiO_2-600, thereby substantiating the presence of mixed phase in TiO_2 samples deposited at higher temperature.[13,22]

UV-vis absorption spectra of all films (Fig. 1f) demonstrate relatively strong absorption in the UV region, whereby the absorption edge is located at about 400 nm.[7,8] The TiO_2-400 spectrum reveals an obvious absorption tail in the visible region, which is attributable to the high density of oxygen vacancies[43,44] and morphology-induced light scattering effect.[45,46] Besides, the absorption edge of TiO_2-400 also appears at a shorter wavelength due to the existence of pure

6940 | *Catal. Sci. Technol.*, 2023, **13**, 6937–6950

This journal is © The Royal Society of Chemistry 2023

anatase phase in the sample. An increase in annealing temperature of TiO_2 leads to a red shift of the absorption edge, owing to an increase in rutile content as confirmed by XRD.[7,9] Note that oxygen vacancies may also contribute to the narrowing of the band gap due to the involvement of shallow defect energy levels.[43,47,48] As a result, TiO_2-500 exhibits significantly red shifted absorption than TiO_2-600 because of the synergistic effect between the mixed phase and the moderate number of oxygen vacancies. TiO_2-500 also shows obvious improvement in absorption intensity most likely caused by the trapping of scattered light. The band gaps of TiO_2-400, TiO_2-500 and TiO_2-600 estimated from the Tauc plot (Fig. S2†) are 3.36, 3.15, and 3.28 eV, respectively.

FESEM images in Fig. 1g–i depict that TiO_2-400 forms nanoparticles with bifrustum structure having an average length between 150 and 200 nm. Besides, most of the nanoparticles fuse together, signifying poor crystallization degree. In contrast, TiO_2-500 shows that some of the nanoparticles grow into larger and highly crystallized bifrustum structures, while some of the particles convert into nanoflake structures with an average length of 300–800 nm, enlarging the surface area for PEC reaction. The fragments of nanoparticles and nanoflakes can be observed in the TEM image in Fig. S3.† Further increase of the temperature to 600 °C completely converts the nanoparticles into nanoflakes. This transformation of structure can be explained in terms of the crystal growth direction. As elaborated in the XRD section, at the annealing temperature of 400 °C, the particles prefer to grow along the (105) crystal plane, therefore forming bifrustum structures. As the temperature increases, the growth rate of nanoparticles along the (105) plane becomes slower than that along the (211) plane, resulting in the transformation of nanoparticles into nanoflakes. The influence of morphology on the light behavior of the film is represented in the schematic diagram. The mixture of bifrustum nanoparticles and nanoflakes in TiO_2-500 is beneficial for light absorption as the bifrustum nanoparticles increase the optical path length through multiple scattering while the nanoflakes effectively trap the scattered light.[45,46] On the other hand, most of the scattered light in TiO_2-400 is not effectively trapped, whereas a fraction of the light simply passes through the TiO_2-600 sample, as supported by UV-vis spectra.

The corresponding photos of the samples are also displayed in the insets of Fig. 1g–i. The cloudy appearance of all samples looks homogeneous when observed from the surface, implying that the present deposition technique forms a uniform coating. However, the film synthesized at 400 °C appeared to be thinner compared to films subjected to higher temperature. As determined from the profilometer, the average thickness of sample deposited at 400 °C is 711 nm, which is lower than that of the TiO_2 deposited at 500 (1120 nm) and 600 °C (1391 nm). As mentioned before, this is because the low annealing temperature weakly supports the growth of TiO_2. AFM analysis in Fig. S4† depicts that the root mean square (RMS) roughness of the synthesized films

increases with the deposition temperature, where the recorded values are 30.1, 75.7 and 85.9 nm for TiO_2-400, TiO_2-500 and TiO_2-600, respectively. The change in roughness is more prominent between the samples that were fabricated at 400 and 500 °C due to the conversion of bifrustum nanoparticles into nanoflakes, which is congruous with the earlier observation.

PEC performance obtained from linear sweep voltammetry (LSV) demonstrates that TiO_2-400 has a relatively weak photocurrent density of 0.5 mA cm^{-2} at 1.23 V_{RHE} (Fig. 2a). As the deposition temperature increases to 500 °C, a steep increase in photocurrent with respect to potential is observed and the performance remarkably enhances, reaching 2.06 mA cm^{-2}. Moreover, the onset potential experiences a cathodic shift which is indicative of an effective charge carrier separation. In contrast, the photocurrent decreases by 0.6 mA cm^{-2} when the temperature is further increased to 600 °C. Note that the negative shift of the dark current onset potential of TiO_2-400 might be due to the exposure of FTO to the electrolyte.[49] Fig. 2b shows that the ABPE of TiO_2-500 reaches a maximum value of 0.81% at 0.72 V_{RHE}, which is quite impressive for a photoanode with single material. A similar trend of photocurrent density is observed in the chronoamperometric scans under chopped illumination (Fig. 2c). The photocurrent spikes in this curve are associated with recombination behavior between electrons and holes. Fig. S5† provides a better view of the photocurrent spikes, where TiO_2-400 shows the most obvious spike, implying the fastest charge recombination. Conversely, the spikes are not visible in TiO_2-500. This observation is also supported by the evaluation of transient photocurrent decay (Fig. S6†), where longer transient time implies lower recombination rate. According to the calculation method described in our previous work,[50] TiO_2-500 reveals the longest transient decay time (0.086 s), followed by TiO_2-600 (0.070 s) and TiO_2-400 (0.054 s).

Fig. 2d presents the electrochemical impedance spectroscopy (EIS) results of TiO_2 under illumination and the values of all resistances obtained from the fitted curves are compiled in Table S2.† R_1 and R_2 represent the charge transfer resistance in the bulk and at the semiconductor/electrolyte interface, respectively. It is apparent that R_2 plays a significant role in the PEC reaction, whereby the resistance decreases in the order TiO_2-400 > TiO_2-600 > TiO_2-500. Further study on the free-carrier density was conducted using Mott–Schottky analysis as depicted in Fig. 2e. The positive slope of the tangent line validates the n-type nature of the semiconductor.[51,52] A steeper slope generally represents lower free carrier density N_D as confirmed by the calculation in the ESI.† The N_D value of TiO_2 is primarily governed by the concentration of oxygen vacancies. Generally, the point defects associated with oxygen vacancies decrease the coordination number of the neighboring Ti^{4+} ions to Ti^{3+} ions. Each under-coordinated Ti atom consists of an unpaired electron and this electron causes an increase in the number of majority carriers in the bulk of TiO_2.[26] Based on

This journal is © The Royal Society of Chemistry 2023

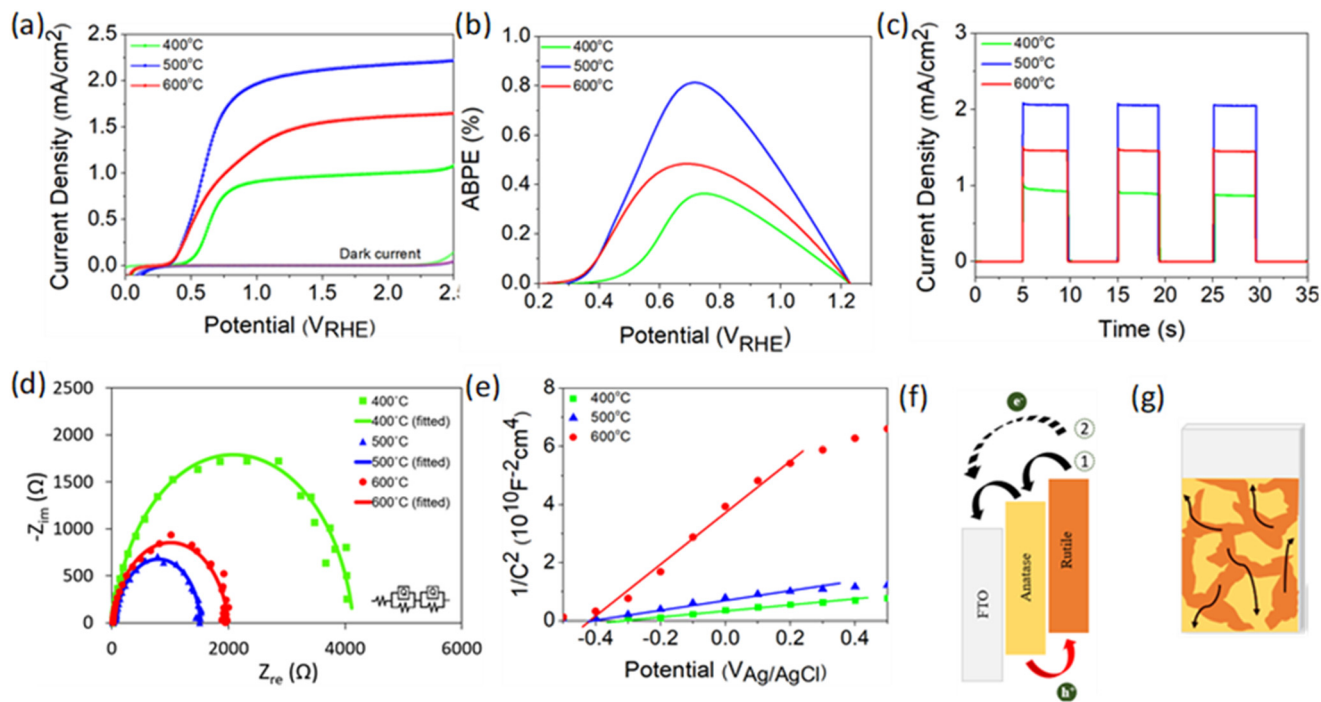*Catal. Sci. Technol.*, 2023, **13**, 6937–6950 | **6941**

Fig. 2 (a) LSV response of TiO_2 deposited at 400, 500 and 600 °C under light and dark conditions and (b) their corresponding ABPE curves. (c) Chronoamperometric scans under chopped illumination and (d) EIS spectra (Nyquist plots) under light illumination measured at a bias voltage of 1.23 V_{RHE}. The inset of (d) shows the equivalent circuit (Voigt circuit) for fitting the curves. (e) Mott–Schottky plots of the respective TiO_2 photoanode. All tests were conducted in 0.5 M Na_2SO_4 electrolyte. (f) Electronic structure of anatase and rutile phases. (g) Schematic diagram of the proposed electron transfer process in the mixed phase TiO_2 photoanode.

the XPS O 1s spectra, the Ti–OH peak clearly reduces with increasing deposition temperature of TiO_2. This observation clarifies the origin of the lower N_D value of fabricated at higher temperature.

From the experimental data above, it is suggested that the enhanced performance of TiO_2-500 is attributed to the synergistic effect between the anatase–rutile mixed phase, appropriate amount of oxygen vacancies and porous structure of the sample. A possible structure of energy band alignment is proposed as in Fig. 2f. Despite the fact that mixed-phase TiO_2 shows better PEC performance than the individual phases, the direction of charge transfer across the phase junction has been controversial.[9,53] This is attributed to the inconsistency of the reported arrangement of the electronic structure between anatase and rutile. Several studies found that the energy band of anatase is higher than that of rutile, whereas some others reported *vice versa*.[8,48,54–57] In this work, the band structure of rutile was found to be higher than that of anatase (see Fig. S7† for more details on the construction of the electronic structure). While photogenerated holes are accumulated in the rutile phase, the electron transfer process may occur in two ways. Firstly, the presence of both phases in this film forms the phase junction or more specifically staggered (type II) heterojunction, which allows the effective transfer of photogenerated electrons from rutile to FTO *via* the anatase phase. Secondly, the electrons from rutile and anatase can also be directly transferred to FTO due to the

random contact of both TiO_2 phases with FTO, as shown in Fig. 2g.

Basically, the mixed phase can suppress the electron–hole recombination by driving the carriers in opposite directions.[7–9,58] This is consistent with the smallest charge transfer resistance of TiO_2-500 observed in EIS spectra. Note that the anatase phase does not only offer the separation path for electron–hole pairs, but the water splitting reaction also occurs at the surface of both anatase and rutile phases, as proven by the DFT calculation in a later section. The DFT analysis reveals that the presence of oxygen vacancies in the sample provides reactive sites for PEC activity. The appropriate amount of oxygen vacancies in TiO_2-500 induces higher free carrier density which can facilitate the PEC activity of the photoanode. Along with the oxygen vacancies, the introduction of rutile in TiO_2-500 leads to a narrow band gap which benefits the light absorption ability. Furthermore, the combination of bifrustum nanoparticles and nanoflakes enhances the light scattering and trapping effects. The high porosity of nanoflake structures of TiO_2-500 also provides a large surface area for photocatalytic reaction and thereby increases the charge transfer rate between the TiO_2 photoanode and the electrolyte.[59]

Meanwhile, the absence of an anatase–rutile mixed phase junction in TiO_2-400 film is detrimental to the charge transfer of TiO_2. Moreover, an excessive number of oxygen vacancies in TiO_2-400 may serve as recombination centers which further deteriorate the charge transfer process.[60] As

6942 | *Catal. Sci. Technol.*, 2023, **13**, 6937–6950

This journal is © The Royal Society of Chemistry 2023

proven by the calculation of transient decay time above, it is clearly seen that TiO$_2$-400 suffers from the highest recombination rate. Besides that, from the viewpoint of morphological properties, the nanoparticle structure of TiO$_2$-400 also reduces the available active sites. On the other hand, the PEC performance of TiO$_2$-600 reduces again, despite the mixed phase and large surface area of the film. This could be ascribed to the poor light trapping induced by the morphology (see FESEM and UV-vis) and low free carrier density induced by low number of oxygen vacancies (see XPS and Mott–Schottky). The low carrier density causes a reduction of electrical conductivity and eventually increases the charge transfer resistance as detected by EIS measurement.[61–63] Another possible reason for the decrease

in photocurrent density may be the deterioration of FTO caused by high annealing temperature.[64–66] However, Hall measurement in Table S3† shows negligible change in the electrical properties of FTO before and after annealing, implying that the performance degradation of TiO$_2$-600 is not attributable to the damage of the substrate.

To evaluate the water splitting reaction on the surface of anatase and rutile, DFT calculation was performed on two main TiO$_2$ surfaces as detected from XRD, namely anatase (101) and rutile (110). The optimized structures of the two surfaces and atom-type labeling are illustrated in Fig. 3a. Anatase (101) provides the characteristic of a terrace-like structure with surface edges constructed by 5-coordinated titanium atoms (Ti$_{5c}$) and 2-coordinated oxygens (O$_{2c}$). These
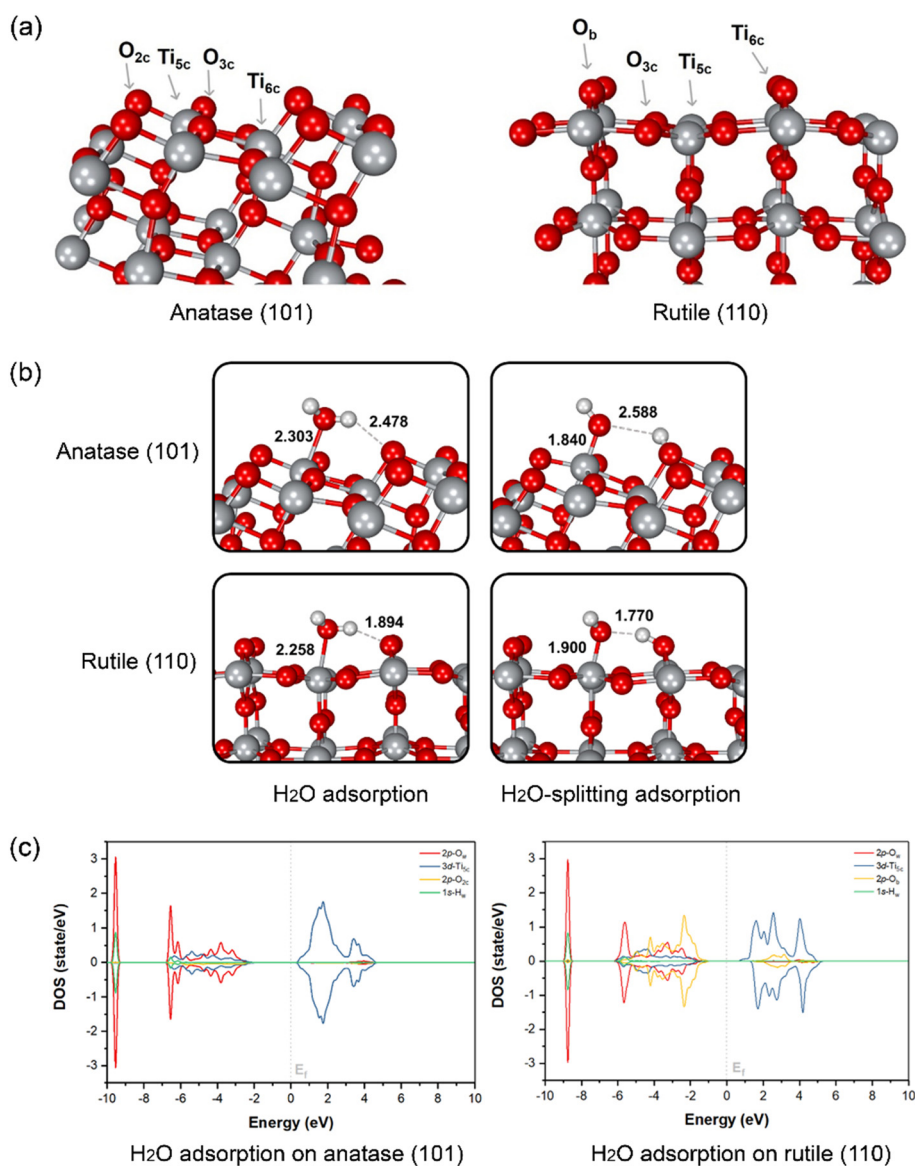

Fig. 3 (a) Optimized structure of TiO$_2$ anatase (101) and rutile (110) facets with labeled surface atoms. (b) Molecular and dissociative adsorption of water on the anatase (101) and rutile (110) surface. The water molecule is adsorbed molecularly (left) and consequently split to OH$^-$ that adsorbs on Ti$_{5c}$ and H$^+$ that adsorbs on O$_{2c}$/O$_b$ (right). Titanium, oxygen and hydrogen atoms are displayed in gray, red and white, respectively. (c) The partial density of states (PDOS) plots of water adsorption on anatase (101) and rutile (110). The Fermi level is marked by a gray dashed line.

undercoordinated atoms are revealed to the interface and it can interact directly with water. In addition, 3-coordinated oxygen (O_{3c}) is found to be the surface interconnecting rows of Ti_{5c}. At the bottom part of the ridges, the 6-coordinated titanium (Ti_{6c}) is disclosed, interacting with O_{3c}. Nevertheless, either O_{3c} or Ti_{6c} is less crucial for interaction with water due to its fully saturated chemical valences by bonding within the TiO_2 structure. Another type of TiO_2 obtained from our synthesis is rutile (110), which is thermodynamically more stable than the anatase form.[67] This plane consists of O_{3c}, Ti_{5c}, and Ti_{6c} atoms. Bridging oxygen atoms (O_b) are illustrated above the rows of bridging. In this case, Ti_{5c} and O_b are reactive sites for water splitting on this surface.

The water and OH^-/H^+ adsorption on either anatase (101) or rutile (110) facets for PEC water splitting reaction were further investigated. In the molecular-adsorption calculations, there are three water adsorption types on the first hydration layer of the anatase (101) surface, which has a characteristic triple-peak pattern in its density profile.[68] First, water hydrogen-bonding to two neighboring O_{2c} by its H_w atoms has been recognized. The second type of water adsorption is that water is hydrogen-bonded via only one of

its H_w to surface O_{2c} while another H_w can interact with other water molecules in the interface region through H-bonding. Lastly, the most stable water adsorption type on the anatase (101) facet is that the water interacts with the surface by its O_w with the unsaturated surface Ti_{5c} site, which is consistent with a previous work.[67]

The interaction between water and anatase is also confirmed via partial density of states (PDOS) plots. It is clearly shown that there is a strong hybridization between the 3d-orbital of Ti_{5c} and the 2p-orbital of O_w. Moreover, water adsorption is slightly stabilized by hydrogen bonding between its H_w and the nearest O_{2c} of the surface with a bond distance of 2.478 Å, as confirmed by the hybridization between the 1s-orbital of H_w and the 2p-orbital of O_{2c} (Fig. 3c). The dissociation of a single water molecule has also been studied as depicted in the top panel of Fig. 3b. H_2O-splitting adsorption occurs when the proton moves to form H-bonding with O_{2c} while negatively charged hydroxyl (OH^-) locates coordinated to Ti_{5c} with a bond length of 1.840 Å above the Ti_{5c} layer. In the case of rutile (110), the water molecular arrangement is presented in the bottom panel of Fig. 3b. The first hydration layer is composed of two main interactions, which are water coordinated by O_w to surface
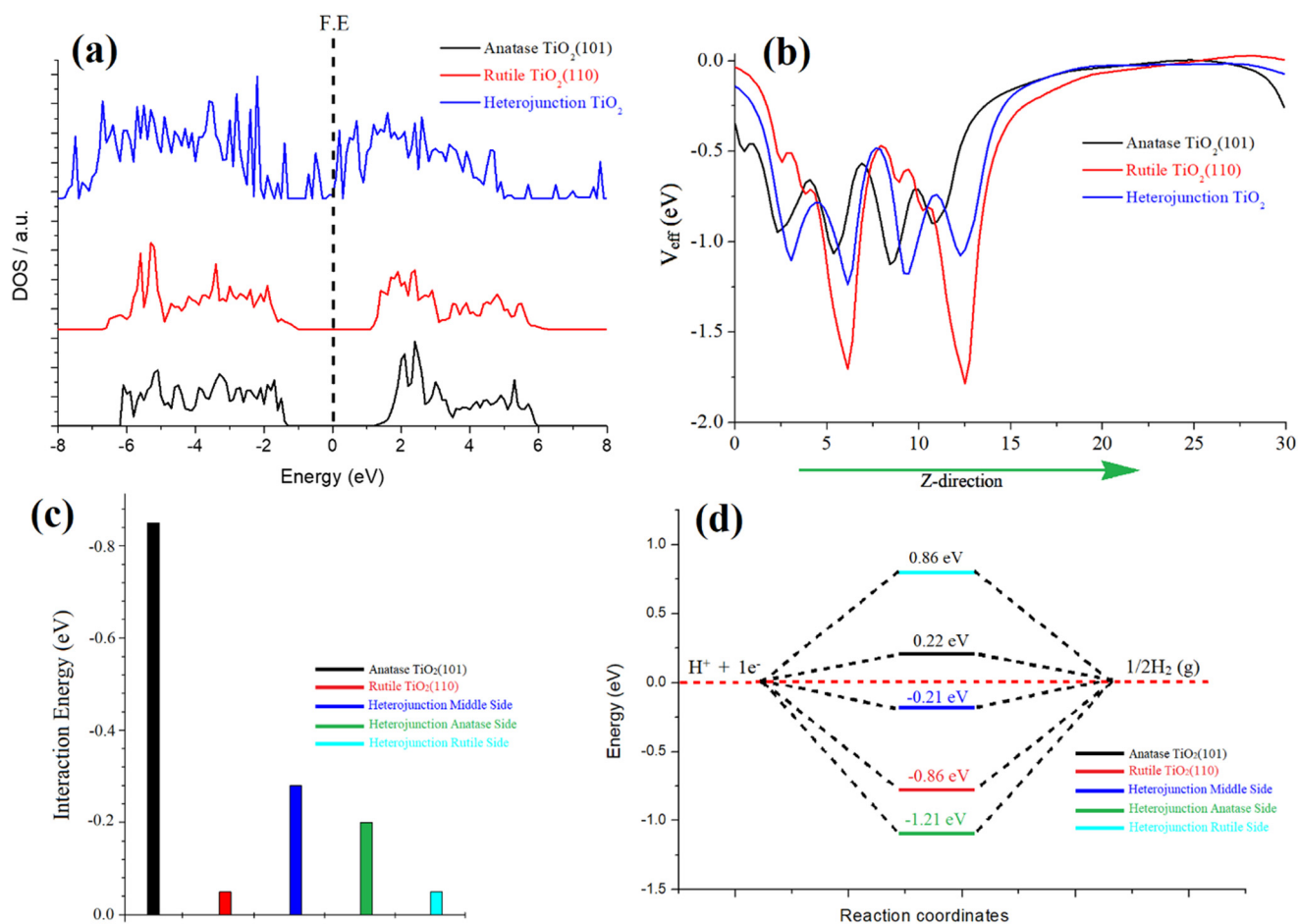

Fig. 4 (a) Comparative DOS, (b) 2D plot of effective potential, (c) water adsorption energy, and (d) free energy diagram of H* adsorption over the surfaces of anatase TiO_2 (101), rutile TiO_2 (110), and heterojunction TiO_2, respectively.

6944 | *Catal. Sci. Technol.*, 2023, **13**, 6937–6950

This journal is © The Royal Society of Chemistry 2023

Ti$_{5c}$ and water hydrogen-bonded by H$_w$ to bridging O$_b$ atoms with bond distances of 2.258 and 1.894 Å, respectively. From the PDOS analysis, we found a strong hybridization between the 3d-orbital of Ti$_{5c}$ and the 2p-orbital of O$_w$. Remarkably, the 2p-orbital of O$_b$ strongly hybridizes the 1s-orbital of H$_w$ at the region of −6 to −2 eV, indicating the hydrogen-bonding between water and rutile (110). The Ti$_{5c}$-coordinated water splitting is observed when the proton of water moves to the nearest bridging O$_b$. The bond length of adsorbed OH$^-$ on Ti$_{5c}$ is 1.900 Å, while that of H$^+$ deposited on the O$_b$ of rutile (110) surface is 1.770 Å. The mechanism of water dissociation and OH$^-$/H$^+$ adsorption at the surface is in good agreement with previous ReaxFF studies of titania surfaces.[69–71]

In our investigation, we focused on the anatase–rutile heterojunction, a composite material comprising anatase and rutile phases. This heterojunction possesses a type II band alignment, resulting in an amplified photocatalytic activity of TiO$_2$. To elucidate the underlying reasons behind this enhanced activity, we conducted simulations of the density of states (DOS) for individual anatase and rutile and the heterojunction, as depicted in Fig. 4a. Notably, the DOS analysis revealed the emergence of additional bands near the Fermi energy within the heterojunction, indicating a pronounced hybridization between the atoms of rutile and anatase TiO$_2$. This strong hybridization effect led to a reduction in the band gap, ultimately enhancing the catalytic activity of the heterojunction. Furthermore, we also simulated the optical spectra for these three species, revealing a narrower optical band gap specifically observed in the heterojunction, as depicted in Fig. S8 of the ESI.†

The phenomenon of charge transformation within the heterojunction is visually evident through the effective potential map, as depicted in Fig. 4b. The potential map reveals a transfer of charge from rutile TiO$_2$ to anatase TiO$_2$. This is manifested by the comparatively more negative red line representing rutile, in contrast to the black line representing anatase. The effective potential of the heterojunction reaches an optimum state, signifying electron transfer to anatase and resulting in an optimized species. Furthermore, this charge transformation is further supported by the electron localization function (ELF) and electron density difference (EDD) plots. The ELF and EDD plots demonstrate excellent interaction/hybridization of electron cloud densities between the atoms, as shown in Fig. S9 and S10 in the ESI.†

To evaluate the water adsorption energy over the surfaces of the three species, we considered the energies of the isolated water molecule, the clean surface, and the water-covered surface. This involved subtracting these energies according to eqn (5). For anatase TiO$_2$(101), the calculated water adsorption energy is −0.85 eV, indicating a strong binding of water molecules to this surface. This suggests a robust interaction between water and the anatase surface. For rutile TiO$_2$ (110), the calculated water adsorption energy is −0.5 eV, indicating a moderate binding of water molecules to this surface. Water exhibits a moderately strong

interaction with the rutile surface. Regarding the anatase–rutile heterojunction, the analysis reveals three potential sites for water adsorption: anatase, rutile, and the middle sites, as depicted in Fig. S11 in the ESI.†

The water adsorption energies at the anatase, rutile, and middle sites of the heterojunction are found to be −0.20 eV, −0.05 eV, and −0.28 eV, respectively. These values indicate the strength of the water binding to the respective sites, with the middle site exhibiting the strongest interaction.

In the context of the hydrogen evolution reaction (HER), we conducted investigations on the properties of anatase, rutile, and the three possible sites of the heterojunction (rutile, anatase, and middle). Introduction of an H atom and subsequent optimization were performed for each case. The HER mechanism was analysed using a three-state diagram encompassing the initial H$^+$ state, intermediate H* state, and 1/2H$_2$ state. The free energy of the H* state (ΔG_{H*}) was found to be a crucial factor in describing the HER activity of the catalyst. It is notable that Pt-based catalysts typically exhibit a ΔG_{H*} value close to 0.09 eV, representing optimal HER performance.

To determine the ΔG_{H*} value, we utilized eqn (6), which incorporates various factors. ΔE represents the total energy change obtained from density functional theory (DFT) simulations, T denotes the temperature (298.15 K for room temperature), and ΔE_{ZPE} and ΔS represent the changes in zero-point energy and entropy, respectively.

$$\Delta G_{H*} = \Delta E_{H*} + \Delta E_{ZPE} - T_{\Delta SH} \quad (6)$$

To simplify the theoretical analysis, we assumed a pH of 0, as the theoretical working potential does not depend on pH. The free energy of hydrogen at standard temperature and pressure (STP) was approximated as the energy of 1/2H$_2$, and the entropy of H$_2$ was obtained from the National Institute of Technology (NIST) database. In eqn (7), ΔE_{H*} corresponds to the binding energy of the adsorbed hydrogen. $E_{(H*)}$ and $E_{(*)}$ represent the energies of the surface with and without H adsorption, respectively, while E_{H_2} represents the DFT energy of molecular H$_2$ in the gas phase.

$$\Delta E_{H*} = E_{(H*)} - E_{(*)} - 1/2E_{H_2} \quad (7)$$

Eqn (8) can be employed to calculate the free energy of H:

$$\Delta G_{H*} = \Delta E_{H*} + 0.37 \text{ eV} \quad (8)$$

The Gibbs free energy (ΔG_{H*}) values were calculated for pristine anatase TiO$_2$ (101) (0.22 eV) and rutile TiO$_2$ (110) (−0.86 eV), as shown in Fig. 4d. Additionally, the heterojunction's anatase, rutile, and middle sites were considered (Fig. S11†). The calculated ΔG_{H*} values for the heterojunction were −1.21 eV (anatase site), 0.86 eV (rutile site), and −0.21 eV (middle of the junction site). Notably, the heterojunction, particularly the middle site, demonstrated an optimal value for the hydrogen evolution reaction (HER). This

This journal is © The Royal Society of Chemistry 2023

Catal. Sci. Technol., 2023, **13**, 6937–6950 | **6945**

indicates that the heterojunction's combined structure of anatase and rutile phases creates more favorable conditions for the HER process compared to individual anatase or rutile surfaces. The charge transfer from rutile to anatase plays a crucial role in enhancing the HER performance of the heterojunction.

Morphological control

The morphology and thickness of TiO_2 films are further controlled by regulating (1) the distance between the nozzle tip and the FTO surface d and (2) the deposition time. The distance was varied between 2, 8 and 15 mm, while the deposition time and temperature were kept constant at 5 min and 500 °C, respectively. A schematic drawing of different nozzle-to-FTO distances and the corresponding FESEM images are shown in Fig. 5a–f. TiO_2 fabricated at d = 2 mm forms nanoparticles with bifrustum structure having a wide

range of sizes which are distributed over the entire substrate. As the distance was extended to 8 mm, a mixture of nanoparticles and nanoflakes are formed, resulting in an increase in the surface roughness and porosity. On the other hand, a compact surface composed of inhomogeneous shard-like particles is obtained when d = 15 mm. From the evaluation of PEC performance (Fig. 5g), the highest photocurrent density of 2.06 mA cm^{-2} at 1.23 V_{RHE} was acquired for TiO_2 deposited at d = 8 mm. Thus, it implies that a more porous surface results in a superior performance.

At a fixed nozzle-to-FTO distance of 8 mm and temperature of 500 °C, a range of deposition times (3, 5 and 7 min) for fabricating TiO_2 were further studied aiming to tune the thickness of the film. The average profilometer measurements of TiO_2 deposited for 3, 5 and 7 min are 610, 1120 and 1362 nm, respectively, whereby TiO_2 deposited for 5 min gives the best PEC performance (Fig. 5h). ABPE for every sample is shown in Fig. S12a and b.† It is known that the
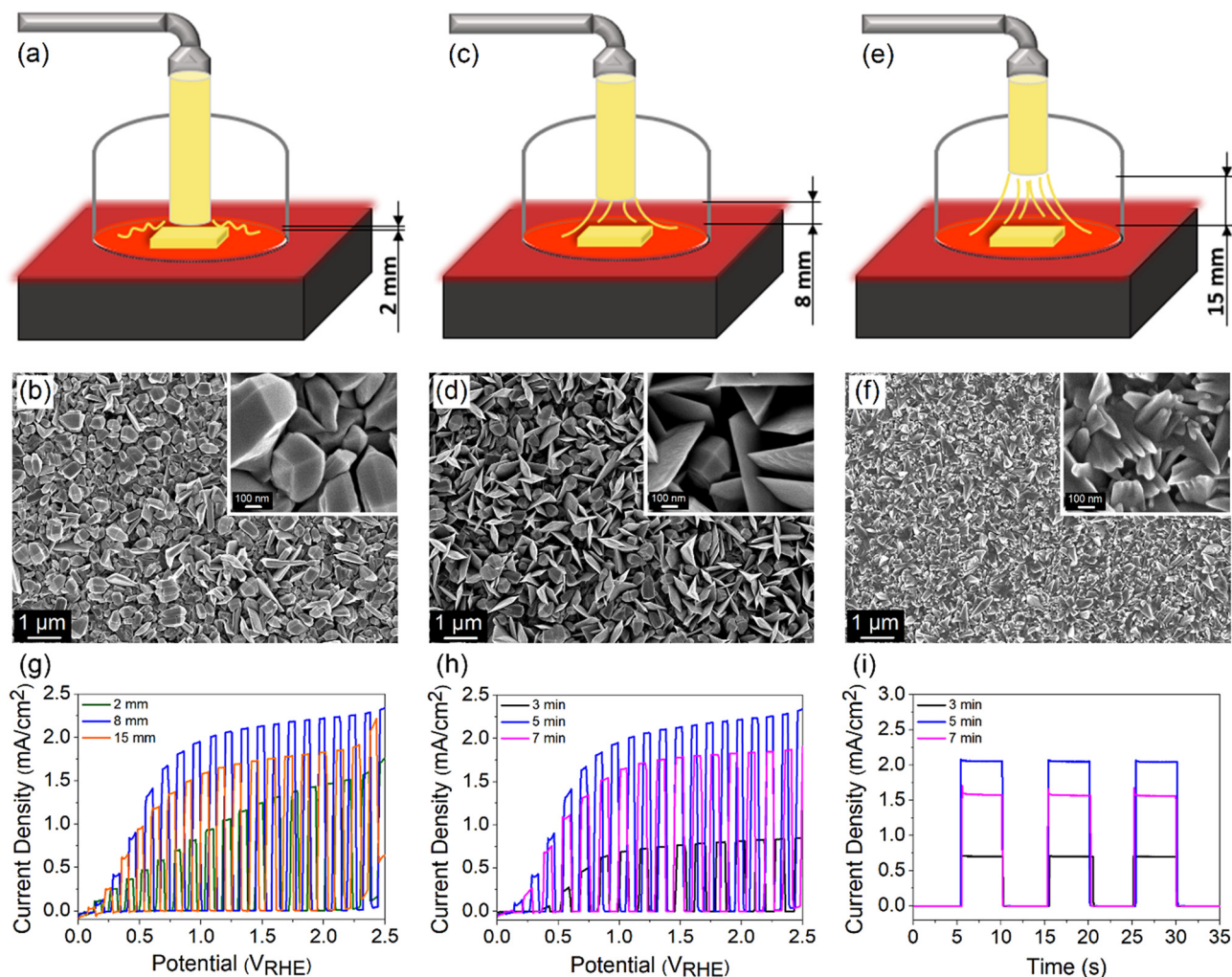

Fig. 5 Schematic drawing and the corresponding FESEM images observed at different magnification scales for TiO_2 deposited at a nozzle-to-FTO distance of (a and b) 2 mm, (c and d) 8 mm and (e and f) 15 mm. The insets in b, d and f show high resolution images. LSV response of TiO_2 photoanode prepared from (g) different nozzle-to-FTO distances and (h) different deposition times. (i) Chronoamperometric scans of TiO_2 photoanode prepared from different deposition times under chopped illumination measured at a bias voltage of 1.23 V_{RHE}.

6946 | *Catal. Sci. Technol.*, 2023, **13**, 6937–6950

This journal is © The Royal Society of Chemistry 2023

PEC activity is also governed by the light absorption and charge carrier diffusion length, both of which correlate strongly with the film thickness. A thin TiO_2 layer deposited for 3 min ineffectively absorbs light which leads to a low number of photogenerated charge carriers. In contrast, excessive thickness obtained from a long deposition time of 7 min may suffer from high charge recombination owing to the limited charge carrier diffusion length. This is reflected in the obvious photocurrent spike in the chronoamperometric scan of the sample deposited for 7 min (Fig. 5i). A balance between the optical and electrical properties explains the origin of the high PEC performance for 5 min-deposited TiO_2 photoanode.

Practicability of APCVD

To move further towards practical implementation in solar hydrogen production, a fabrication process capable of producing an efficient photoelectrode with high consistency is imperative. Therefore, the consistency of the developed APCVD method for growing TiO_2 in this work was further scrutinized by fabricating 20 photoanodes under optimized deposition parameters. As presented in Fig. 6a, the average current density measured at 1.23 V_{RHE} is 1.86 mA cm^{-2}, which is merely 10% deviation from the champion sample. Moreover, TiO_2 demonstrates relatively stable performance with high photocurrent output over 16 h of continuous

operation under irradiation (Fig. 6b). The PEC activity of the photoanode was also verified by measuring the generated hydrogen and oxygen gases during the stability test. Fig. 6c shows that approximately 138 μmol of H_2 and 62 μmol of O_2 are produced after 16 h of illumination, which are in close agreement with the theoretical values. The LSV curve of the champion TiO_2 photoanode was also taken randomly from time to time. Surprisingly, the sample retains 97% of the initial photocurrent density at 1.23 V_{RHE} even after 3 years of storage under ambient conditions (Fig. 6d), signifying the magnificent stability of the photoanode against standard environmental stress.

Additionally, a variety of preparation approaches carried out for depositing TiO_2 photoanode is summarized in Table S4† to provide a comparison between this work and the available fabrication methods. Most of the synthesis methods reported to date not only involved multiple deposition protocols but also used various types of chemicals. This may reduce the energy- and cost-effectiveness of photoelectrode production. Besides, those methods took several hours to obtain high-performance TiO_2 which is basically unsuitable for industrial implementation of PEC technology in the future. On the other hand, the reasonable performance, excellent reproducibility and high stability of the TiO_2 photoanode prepared in this work from a single reagent (*i.e.*, $TiCl_4$ only) using a single deposition technique (*i.e.*, APCVD) under a very short time-scale (*i.e.*, 5 min) offers a remarkable
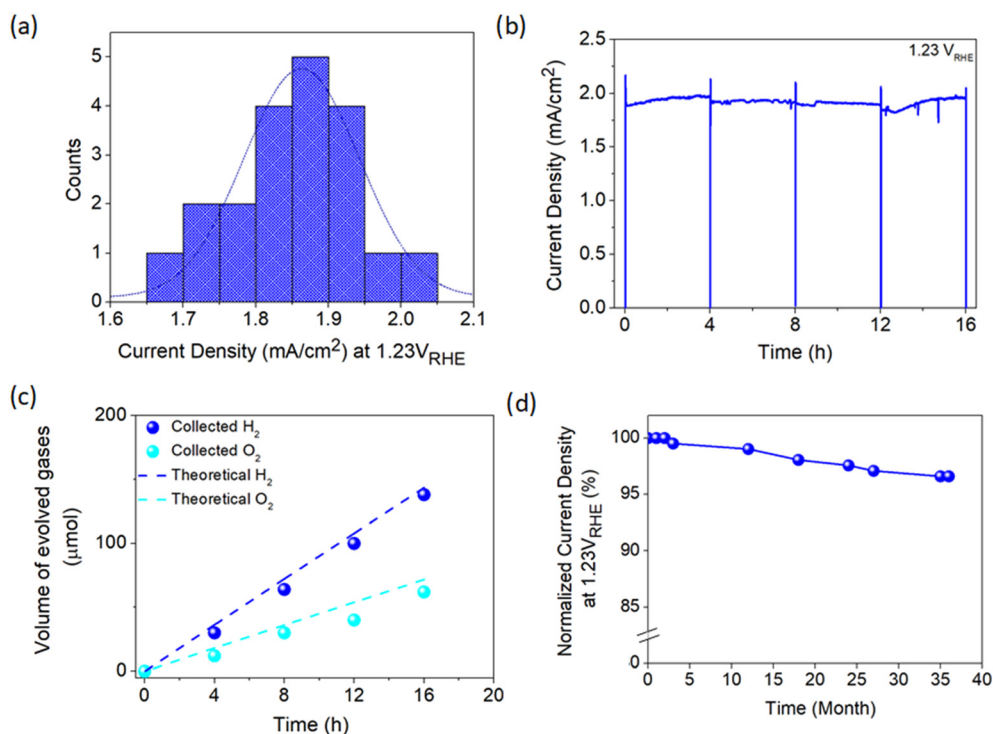

Fig. 6 (a) Distribution of the measured photocurrent density at 1.23 V_{RHE} for 20 photoanodes prepared under optimized deposition conditions. (b) Photostability evaluation of anatase–rutile TiO_2 photoanode at 1.23 V_{RHE} under light illumination over 4 consecutive scans with each scan lasting 4 h and (c) the corresponding H_2 and O_2 gas evolution. (d) Long-term stability of TiO_2 photoanode stored under ambient conditions measured at irregular time intervals over 3 years.

breakthrough in PEC water splitting application. A TiO$_2$ photoanode with an area of l6 cm^2 (4 × 4 cm) has also been developed, which is the largest area achievable using our laboratory system set-up. Despite the experimental limitation and mediocre film quality (Fig. S13a†), a photocurrent density of 0.77 mA cm^{-2} at 1.23 V$_{RHE}$ is still attainable (Fig. S13b†) which is around 40% of the 1 cm^2-sized sample. This suggests the practicability of the present work, but further development is needed to enhance the performance of large-area photoanodes closer to the optimum value.

Conclusion

In summary, an efficient TiO$_2$ photoanode was successfully developed using a rapid deposition technique (5 min) based on a custom-built APCVD system and by employing TiCl$_4$ as a single reagent. The crystal phase, defect density, morphology and thickness of TiO$_2$ films have been rationally tuned to acquire the optimum deposition conditions. The formation of a staggered junction between anatase and rutile phases in TiO$_2$ significantly improves electron–hole separation and suppresses charge recombination. An appropriate number of oxygen vacancies provides high free carrier density and prevents the formation of undesirable recombination centers. DFT analysis also proves that the undercoordinated Ti and O atoms in both anatase and rutile phases serve as active sites for photocatalytic reaction. Furthermore, an intriguing observation reveals that the TiO$_2$ heterojunction exhibits superior hydrogen evolution reaction (HER) performance, primarily attributed to its optimized Gibbs free energy compared to pure rutile and anatase. This enhancement can be attributed to the transfer of charges from rutile to anatase, resulting in an amplified HER performance within the heterojunction. Besides, the mixture of bifrustum nanoparticles and nanoflakes provide a unique light trapping effect and large active sites. Moreover, appropriate thickness ensures a balance between light absorption and charge diffusion length. The best photoanode not only reveals a high and stable photocurrent of 2.06 mA cm^{-2} at 1.23 V$_{RHE}$ but also yields 138 μmol of H$_2$ and 62 μmol of O$_2$ over 16 h of PEC operation. The discovery in this study may be a valuable guide for designing, developing and commercializing sustainable PEC technology.

Author contributions

Nurul Affiqah Arzaee: investigation, writing – original draft, writing – review & editing. Nuttapon Yodsin, Siriporn Jungsuttiwong, Habib Ullah, and Sabiha Sultana: methodology, software. Mohamad Firdaus Mohamad Noh and Ahmad Wafi Mahmood Zuhdib: formal analysis, validation. Abd Rashid Bin Mohd Yusoff: resources: formal analysis, validation. Mohd Asri Mat Teridi: supervision, conceptualization, funding acquisition.

Conflicts of interest

The authors declare that they have no known competing financial interests or personal relationships that could have appeared to influence the work reported in this paper.

Acknowledgements

References

1 Z. Chen, A. J. Corkett, C. de Bruin-Dickason, J. Chen, A. Rokicińska, P. Kuśtrowski, R. Dronskowski and A. Slabon, *Inorg. Chem.*, 2020, **59**, 13589–13597.

2 N. A. Mohamed, J. Safaei, A. F. Ismail, M. F. Mohamad Noh, N. A. Arzaee, N. N. Mansor, M. A. Ibrahim, N. A. Ludin, J. S. Sagu and M. A. Mat Teridi, *J. Alloys Compd.*, 2019, **818**, 152916.

3 H. Zheng, L. Zheng, X. Ye, X. Deng, Y. Wang, Y. Zhao and X. Shi, *ACS Sustainable Chem. Eng.*, 2020, **8**, 15906–15914.

4 Z. Liang, H. Hou, Z. Fang, F. Gao, L. Wang, D. Chen and W. Yang, *ACS Appl. Mater. Interfaces*, 2019, **11**, 19167–19175.

5 T. Zhou, J. Wang, S. Chen, J. Bai, J. Li, Y. Zhang, L. Li, L. Xia, M. Rahim, Q. Xu and B. Zhou, *Appl. Catal., B*, 2020, **267**, 118599.

6 X. Cheng, Y. Zhang, H. Hu, M. Shang and Y. Bi, *Nanoscale*, 2018, **10**, 3644–3649.

7 J. Hu, S. Zhang, Y. Cao, H. Wang, H. Yu and F. Peng, *ACS Sustainable Chem. Eng.*, 2018, **6**, 10823–10832.

8 F. Cao, J. Xiong, F. Wu, Q. Liu, Z. Shi, Y. Yu, X. Wang and L. Li, *ACS Appl. Mater. Interfaces*, 2016, **8**, 12239–12245.

9 A. Li, Z. Wang, H. Yin, S. Wang, P. Yan, B. Huang, X. Wang, R. Li, X. Zong, H. Han and C. Li, *Chem. Sci.*, 2016, **7**, 6076–6082.

10 A. Ghobadi, T. G. Ulusoy, R. Garifullin, M. O. Guler and A. K. Okyay, *Sci. Rep.*, 2016, **6**, 30587.

11 S. Jia, X. Shu, H. Song, Z. An, X. Xiang, J. Zhang, Y. Zhu and J. He, *Ind. Eng. Chem. Res.*, 2021, **60**, 12282–12291.

12 J. S. Yang and J. J. Wu, *ACS Appl. Mater. Interfaces*, 2018, **10**, 3714–3722.

13 H. Sutiono, A. M. Tripathi, H. M. Chen, C. H. Chen, W. N. Su, L. Y. Chen, H. Dai and B. J. Hwang, *ACS Sustainable Chem. Eng.*, 2016, **4**, 5963–5971.

14 N. Wei, Y. Liu, M. Feng, Z. Li, S. Chen, Y. Zheng and D. Wang, *Appl. Catal., B*, 2019, **244**, 519–528.

15 Q. Kang, J. Cao, Y. Zhang, L. Liu, H. Xu and J. Ye, *J. Mater. Chem. A*, 2013, **1**, 5766.

6948 | *Catal. Sci. Technol.*, 2023, **13**, 6937–6950

This journal is © The Royal Society of Chemistry 2023

16 X. Lv, L. Tao, M. Cao, X. Xiao, M. Wang and Y. Shen, *Nano Energy*, 2018, **44**, 411–418.

17 I. Cesar, K. Sivula, A. Kay, R. Zboril and M. Grätzel, *J. Phys. Chem. C*, 2009, **113**, 772–782.

18 P. Carmichael, D. Hazafy, D. S. Bhachu, A. Mills, J. A. Darr and I. P. Parkin, *Phys. Chem. Chem. Phys.*, 2013, **15**, 16788–16794.

19 C. Sotelo-Vazquez, R. Quesada-Cabrera, J. A. Darr and I. P. Parkin, *J. Mater. Chem. A*, 2014, **2**, 7082.

20 A. Kafizas, N. Noor, P. Carmichael, D. O. Scanlon, C. J. Carmalt and I. P. Parkin, *Adv. Funct. Mater.*, 2014, **24**, 1758–1771.

21 A. Kafizas, X. Wang, S. R. Pendlebury, P. Barnes, M. Ling, C. Sotelo-Vazquez, R. Quesada-Cabrera, C. Li, I. P. Parkin and J. R. Durrant, *J. Phys. Chem. A*, 2016, **120**, 715–723.

22 M. Chandra and D. Pradhan, *ChemSusChem*, 2020, **13**, 3005–3016.

23 S. Wang, T. He, J. H. Yun, Y. Hu, M. Xiao, A. Du and L. Wang, *Adv. Funct. Mater.*, 2018, **28**, 1–10.

24 M. Kuang, P. Han, Q. Wang, J. Li and G. Zheng, *Adv. Funct. Mater.*, 2016, **26**, 8555–8561.

25 J. Safaei, H. Ullah, N. A. Mohamed, M. F. Mohamad Noh, M. F. Soh, A. A. Tahir, N. Ahmad Ludin, M. A. Ibrahim, W. N. R. Wan Isahak and M. A. Mat Teridi, *Appl. Catal., B*, 2018, **234**, 296–310.

26 M. F. Mohamad Noh, H. Ullah, N. A. Arzaee, A. Ab Halim, M. A. F. Abdul Rahim, N. A. Mohamed, J. Safaei, S. N. F. Mohd Nasir, G. Wang and M. A. Mat Teridi, *Dalton Trans.*, 2020, **49**, 12037–12048.

27 G. Kresse and D. Joubert, *Phys. Rev. B: Condens. Matter Mater. Phys.*, 1999, **59**, 1758–1775.

28 J. Paier, R. Hirschl, M. Marsman and G. Kresse, *J. Chem. Phys.*, 2005, **122**, 234102.

29 S. Yu, B. Han, Y. Lou, G. Qian and Z. Wang, *Inorg. Chem.*, 2020, **59**, 3330–3339.

30 N. A. Arzaee, M. F. Mohamad Noh, A. Ab Halim, M. A. F. Abdul Rahim, N. A. Mohamed, J. Safaei, A. Aadenan, S. N. Syed Nasir, A. F. Ismail and M. A. Mat Teridi, *Ceram. Int.*, 2019, **45**, 16797–16802.

31 J. Ding, L. Wang, Y. Zhao, X. Yu, L. Xing, G. Ding, J. Zhang and R. Che, *ACS Appl. Mater. Interfaces*, 2020, **12**, 48140–48149.

32 C. Byrne, R. Fagan, S. Hinder, D. E. McCormack and S. C. Pillai, *RSC Adv.*, 2016, **6**, 95232–95238.

33 M. G. Kim, J. M. Kang, J. E. Lee, K. S. Kim, K. H. Kim, M. Cho and S. G. Lee, *ACS Omega*, 2021, **6**, 10668–10678.

34 C. Byrne, L. Moran, D. Hermosilla, N. Merayo, Á. Blanco, S. Rhatigan, S. Hinder, P. Ganguly, M. Nolan and S. C. Pillai, *Appl. Catal., B*, 2019, **246**, 266–276.

35 D. A. H. Hanaor and C. C. Sorrell, *J. Mater. Sci.*, 2011, **46**, 855–874.

36 J. Huang, T. Chen, M. Zhao, P. Yi, F. Zhao, B. He, Y. Wang, Y. Chen, X. Liu and Z. Li, *CrystEngComm*, 2021, **23**, 2952–2960.

37 D. Yoon, S. Yu and J. Son, *NPG Asia Mater.*, 2018, **10**, 363–371.

38 C. A. Aggelopoulos, M. Dimitropoulos, A. Govatsi, L. Sygellou, C. D. Tsakiroglou and S. N. Yannopoulos, *Appl. Catal., B*, 2017, **205**, 292–301.

39 X. Huang, X. Gao, Q. Xue, C. Wang, R. Zhang, Y. Gao and Z. Han, *Dalton Trans.*, 2020, **49**, 2184–2189.

40 J. Li, M. Zhang, Z. Guan, Q. Li, C. He and J. Yang, *Appl. Catal., B*, 2017, **206**, 300–307.

41 H. Cui, W. Zhao, C. Yang, H. Yin, T. Lin, Y. Shan, Y. Xie, H. Gu and F. Huang, *J. Mater. Chem. A*, 2014, **2**, 8612–8616.

42 H. Zhang, J. Cai, Y. Wang, M. Wu, M. Meng, Y. Tian, X. Li, J. Zhang, L. Zheng, Z. Jiang and J. Gong, *Appl. Catal., B*, 2018, **220**, 126–136.

43 M. Kim, B. Lee, H. Ju, J. Y. Kim, J. Kim and S. W. Lee, *Adv. Mater.*, 2019, **31**, 1903316.

44 M. F. Mohamad Noh, N. A. Arzaee, J. Safaei, N. A. Mohamed, H. P. Kim, A. R. Mohd Yusoff, J. Jang and M. A. Mat Teridi, *J. Alloys Compd.*, 2019, **773**, 997–1008.

45 Y. Chen, W. Zheng, S. Murcia-López, F. Lv, J. R. Morante, L. Vayssieres and C. Burda, *J. Mater. Chem. C*, 2021, **9**, 3726–3748.

46 Z. Wang, H. Zhu, W. Tu, X. Zhu, Y. Yao, Y. Zhou and Z. Zou, *Adv. Sci.*, 2022, **9**, 2103744.

47 X. Zhang, L. Luo, R. Yun, M. Pu, B. Zhang and X. Xiang, *ACS Sustainable Chem. Eng.*, 2019, **7**, 13856–13864.

48 C. Ai, P. Xie, X. Zhang, X. Zheng, J. Li, A. Kafizas and S. Lin, *ACS Sustainable Chem. Eng.*, 2019, **7**, 5274–5282.

49 P. Dias, T. Lopes, L. Meda, L. Andrade and A. Mendes, *Phys. Chem. Chem. Phys.*, 2016, **18**, 5232–5243.

50 N. A. Arzaee, M. F. Mohamad Noh, N. S. H. Mohd Ita, N. A. Mohamed, S. N. F. Mohd Nasir, I. N. Nawas Mumthas, A. F. Ismail and M. A. Mat Teridi, *Dalton Trans.*, 2020, **49**, 11317–11328.

51 L. Luo, T. Zhang, X. Zhang, R. Yun, Y. Lin, B. Zhang and X. Xiang, *Catalysts*, 2020, **10**, 539.

52 N. A. Arzaee, M. F. Mohamad Noh, A. Aadenan, I. N. Nawas Mumthas, F. F. Ab Hamid, N. N. Kamarudin, N. A. Mohamed, M. A. Ibrahim, A. F. Ismail and M. A. Mat Teridi, *Chem. Eng. Sci.*, 2021, 117294.

53 W. N. Zhao, S. C. Zhu, Y. F. Li and Z. P. Liu, *Chem. Sci.*, 2015, **6**, 3483–3494.

54 D. Wang, X. Zhang, P. Sun, S. Lu, L. Wang, C. Wang and Y. Liu, *Electrochim. Acta*, 2014, **130**, 290–295.

55 P. Sun, X. Zhang, C. Wang, Y. Wei, L. Wang and Y. Liu, *J. Mater. Chem. A*, 2013, **1**, 3309.

56 Z. Liu, X. Zhang, S. Nishimoto, M. Jin, D. A. Tryk, T. Murakami and A. Fujishima, *Langmuir*, 2007, **23**, 10916–10919.

57 M. Meng, L. Yang, J. Yang, Y. Zhu, C. Li, H. Xia, H. Yuan, M. Zhang, Y. Zhao, F. Tian, J. Li, K. Liu, L. Wang and Z. Gan, *J. Colloid Interface Sci.*, 2023, **648**, 56–65.

58 J. S. Yang, W. P. Liao and J. J. Wu, *ACS Appl. Mater. Interfaces*, 2013, **5**, 7425–7431.

59 S. N. F. Mohd Nasir, H. Ullah, M. Abd Mutalib, F. H. Saifuddin, N. A. Arzaee, A. A. Tahir, M. F. Mohamad Noh, M. A. Ibrahim, H. Moria, M. N. Alghamdi and M. A. Mat Teridi, *J. Phys. Chem. C*, 2021, **125**, 27148–27158.

This journal is © The Royal Society of Chemistry 2023

Catal. Sci. Technol., 2023, **13**, 6937–6950 | **6949**

60 Y. Wang and J. M. Wu, *Adv. Funct. Mater.*, 2020, **30**, 1907619.

61 H. Meng, K. Fan, J. Low and J. Yu, *Dalton Trans.*, 2016, **45**, 13717–13725.

62 T. Soltani and B.-K. Lee, *Sci. Total Environ.*, 2020, **736**, 138640.

63 N. A. Arzaee, M. F. Mohamad Noh, A. A. Halim, M. A. F. Abdul Rahim, N. S. H. Mohd Ita, N. A. Mohamed, S. N. F. Mohd Nasir, A. F. Ismail and M. A. Mat Teridi, *J. Alloys Compd.*, 2021, **852**, 156757.

64 D. Wang, Y. Chen, Y. Zhang, X. Zhang, N. Suzuki and C. Terashima, *Appl. Surf. Sci.*, 2017, **422**, 913–920.

65 E. S. Cho, M. J. Kang and Y. S. Kang, *Phys. Chem. Chem. Phys.*, 2015, **17**, 16145–16150.

66 A. Annamalai, A. Subramanian, U. Kang, H. Park, S. H. Choi and J. S. Jang, *J. Phys. Chem. C*, 2015, **119**, 3810–3817.

67 Z. Futera and N. J. English, *J. Phys. Chem. C*, 2017, **121**, 6701–6711.

68 Z. Futera and N. J. English, *J. Phys. Chem. C*, 2016, **120**, 19603–19612.

69 S.-Y. Kim, N. Kumar, P. Persson, J. Sofo, A. C. T. van Duin and J. D. Kubicki, *Langmuir*, 2013, **29**, 7838–7846.

70 M. Raju, S.-Y. Kim, A. C. T. van Duin and K. A. Fichthorn, *J. Phys. Chem. C*, 2013, **117**, 10558–10572.

71 L. Huang, K. E. Gubbins, L. Li and X. Lu, *Langmuir*, 2014, **30**, 14832–14840.

6950 | *Catal. Sci. Technol.*, 2023, **13**, 6937–6950

This journal is © The Royal Society of Chemistry 2023